Ink Design Enabling Slot-Die Coated Perovskite Solar Cells with >22% Power Conversion Efficiency, Micro-Modules, and 1 Year of Outdoor Performance Evaluation

Jinzhao Li,* Janardan Dagar, Oleksandra Shargaieva, Oliver Maus, Marco Remec, Quiterie Emery, Mark Khenkin, Carolin Ulbrich, Fatima Akhundova, José A. Márquez, Thomas Unold, Markus Fenske, Christof Schultz, Bert Stegemann, Amran Al-Ashouri, Steve Albrecht, Alvaro Tejada Esteves, Lars Korte, Hans Köbler, Antonio Abate, Daniel M. Többens, Ivo Zizak, Emil J. W. List-Kratochvil, Rutger Schlatmann, and Eva Unger*

The next technological step in the exploration of metal-halide perovskite solar cells is the demonstration of larger-area device prototypes under outdoor operating conditions. The authors here demonstrate that when slot-die coating the halide perovskite layers on large areas, ribbing effects may occur but can be prevented by adjusting the precursor ink's rheological properties. For formamidinium lead triiodide (FAPbI$_3$) precursor inks based on 2-methoxyethanol, the ink viscosity is adjusted by adding acetonitrile (ACN) as a co-solvent leading to smooth FAPbI$_3$ thin-films with high quality and layer homogeneity. For an optimized content of 46 vol% of the ACN co-solvent, a certified steady-state performance of 22.3% is achieved in p-i-n FAPbI$_3$-perovskite solar cells. Scaling devices to larger areas by making laser series-interconnected mini-modules of 12.7 cm^2, a power conversion efficiency of 17.1% is demonstrated. A full year of outdoor stability testing with continuous maximum power point tracking on encapsulated devices is performed and it is demonstrated that these devices maintain close to 100% of their initial performance during winter and spring followed by a significant performance decline during warmer summer months. This work highlights the importance of the real-condition evaluation of larger area device prototypes to validate the technological potential of halide perovskite photovoltaics.

1. Introduction

Having reached high performance in small-area test devices, demonstrating scalable and stable perovskite solar cells will enable further technological exploration of these materials for photovoltaic applications. Metal-halide perovskite (MHP) semiconductors have various advantages as a photovoltaic material, such as a high absorption coefficient,[1] long carrier diffusion length,[2] low-cost, and low-temperature solution processing.[3] When scaling the solution-based processing of halide perovskites to larger areas, coating inhomogeneities may occur due to rheological effects of the precursor inks leading to layer-thickness inhomogeneities. We here emphasize the importance to develop optimized ink formulations to enable large-area homogeneous coatings of MHP to scale this solar cell technology to module dimensions.

J. Li, J. Dagar, O. Shargaieva, O. Maus, M. Remec, Q. Emery, M. Khenkin, C. Ulbrich, F. Akhundova, J. A. Márquez, T. Unold, M. Fenske, A. Al-Ashouri, S. Albrecht, A. T. Esteves, L. Korte, H. Köbler, A. Abate, D. M. Többens, I. Zizak, E. J. W. List-Kratochvil, R. Schlatmann, E. Unger
Helmholtz-Zentrum Berlin für Materialien und Energie GmbH
Hahn-Meitner-Platz 1, D-14109 Berlin, Germany
E-mail: jinzhao.li@helmholtz-berlin.de; eva.unger@helmholtz-berlin.de

The ORCID identification number(s) for the author(s) of this article can be found under https://doi.org/10.1002/aenm.202203898.

J. Li, E. J. W. List-Kratochvil, E. Unger
Institut für Chemie & IRIS Adlershof
Humboldt-Universität zu Berlin
Zum Großen Windkanal 2, 12489 Berlin, Germany

M. Remec
Faculty of Electrical Engineering
University of Ljubljana
Tržaška cesta 25, Ljubljana 1000, Slovenia

J. A. Márquez, E. J. W. List-Kratochvil
Institut für Physik & IRIS Adlershof
Humboldt-Universität zu Berlin
Zum Großen Windkanal 2, 12489 Berlin, Germany

C. Schultz, B. Stegemann
University of Applied Sciences – HTW Berlin
Wilhelminenhofstr. 75a, D-12459 Berlin, Germany

**ADVANCED
SCIENCE NEWS**

www.advancedsciencenews.com

**ADVANCED
ENERGY
MATERIALS**

www.advenergymat.de

Most process optimization of perovskite solar cells (PSCs) is based on non-scalable spin-coating processes as the main deposition methods.[4,5] Considerable re-engineering of precursor inks and processes has to be carried out when employing scalable fabrication methods, such as inkjet printing,[6] spray coating,[7] vapor-assisted deposition,[8] evaporation,[9] blade coating, and slot-die coating (SDC).[10,11] Among them, the slot-die coating is one of the most promising processes enabling sheet-to-sheet, continuous roll-to-roll coating, and solution-processable optoelectronic device technology such as organic electronic devices and polymer solar cells.[12–14] In our previous work, we demonstrated efficient inverted PSC fabricated by SDC with power conversion efficiencies (PCEs) over 20%.[11] However, it remains far behind the champion device from blade coating.[15] We conclude that one of the challenges in SDC is to control the crystallization of perovskite wet films by optimizing the precursor ink and coating parameters so that a homogenous and pinhole-free film is achieved.[16] Therefore, more efforts are needed in the optimization of precursor solvents to achieve efficient and stable devices.

As a pre-metered coating process, the thickness and quality of slot-die coated wet films (t) are determined by several parameters, which include coating speed (v), flow rate, coating gap (h_0), geometry of the die head, and the precursor ink's rheological properties. Unstable coating conditions due to dripping, air entrenchment, and ribbing may cause layer inhomogeneities in the deposited wet film.[17] Among these, ribbing is a common effect observed at the downstream meniscus when the viscous and capillary forces between ink, slot-die, and substrate are unbalanced.[17] One feasible strategy to minimize ribbing effects is to reduce the viscosity, μ, of the precursor ink or adjust the coating speed while increasing the surface tension to aid in leveling[18,19] (Note S1, Supporting Information).

When processing MHPs from solutions, solvents actually play multiple roles in determining the final thin-film quality during different stages of thin-film growth, illustrated in **Figure 1**. Initially and primarily, solvents are chosen to effectively dissolve precursor salts at sufficiently high concentrations to enable coating thin films thick enough to absorb most incident light (ca. 700 nm in the case of halide perovskites) in a single deposition run. Secondly, during processing, the rheological properties of precursor inks also significantly affect the coating homogeneity during processing. Solvent removal becomes of essence upon depositing precursors from the solution and here the solvent-removal rate, determined by its boiling point/vapor pressure and interaction with the solute(s), critically affects the growth dynamics of the thin film. In addition, solvents may strongly interact with the precursor salts and become incorporated in solvate intermediate phases, which affect the growth mechanism and may template the resulting thin-film morphology. In this regard, it becomes critically important to start distinguishing the role and effect different solvents play during the different stages of processing as illustrated in Figure 1.

Formamidinium lead triiodide (FAPbI₃) has been demonstrated to enable efficient PSCs with a more ideal bandgap for single-junction devices and better thermal stability compared to methylammonium lead triiodide.[20] However, FAPbI₃ readily undergoes a phase transition in ambient conditions from a black cubic α-phase to a yellow non-perovskite δ-phase.[21] The addition of methylammonium hydrochloride (MACl) salt has been previously demonstrated to promote the stabilization of the FAPbI₃ perovskite α-phase due to a more optimal tolerance factor upon the incorporation of the smaller MA cation and Cl anion into the crystal lattice.[22,23] On the other hand, 2-methoxyethanol (2-ME) has been shown to be a solvent with high solubility for dissolving perovskite precursors.[24,25] The boiling point of 2-ME is relatively low, which allows fast solvent removal in the coating of perovskite films and makes it extremely suitable for upscaling methods such as blade
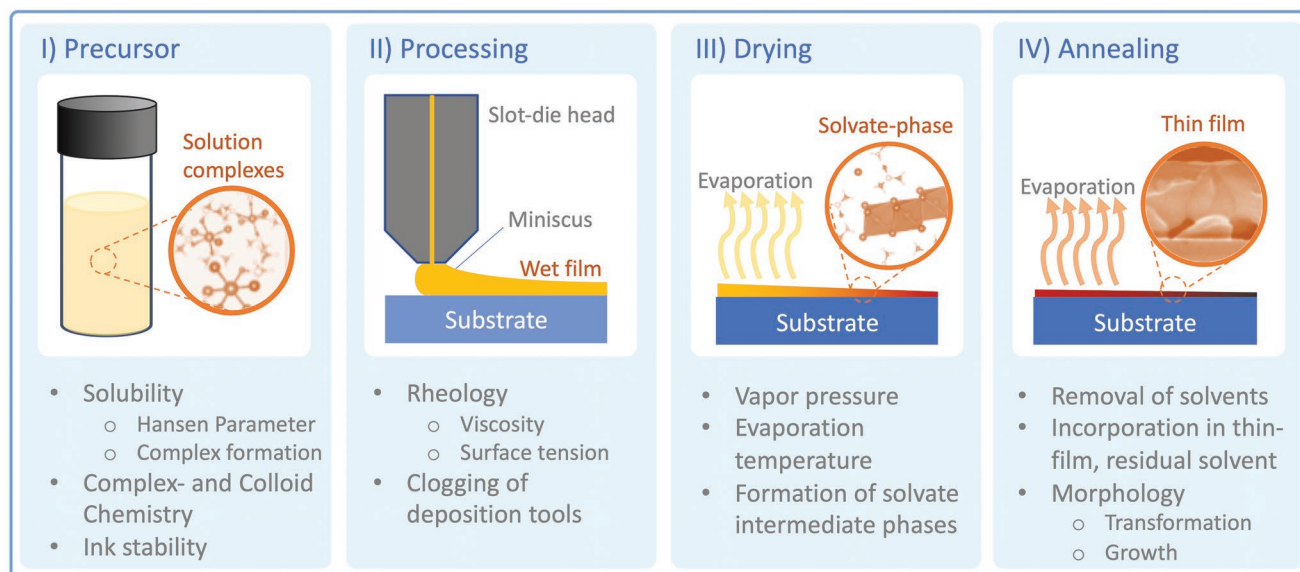
Figure 1. Illustration of different stages and roles of solvents used during thin film processing by solution-based methods such as slot-die coating. Initially, in stage I, solvents are chosen to achieve good solubility of precursor components in often high molar concentrations. During the drying process, stage II, the rheology of the precursor ink critically determines the homogeneity of the coated wet-film. During solvent removal or drying, stage III, solvent molecules need to be removed in a fashion favorable to promote thin film formation during which also solid intermediate phases might form, which are then converted into the final thin-film during annealing (stage IV).

**ADVANCED
SCIENCE NEWS**

www.advancedsciencenews.com

**ADVANCED
ENERGY
MATERIALS**

www.advenergymat.de

coating and slot-die coating.[10,11] Precursor inks investigated here were based on the solvents 2-ME and small amounts of N-methyl-2-pyrrolidone (NMP) introduced as a strongly coordinating co-solvent that was shown to promote the formation of $FAI \cdot PbI_2 \cdot NMP$ adduct.[24,26] The combination of NMP and MACl has been previously demonstrated to be an efficient strategy for obtaining high-quality and black α-phase perovskite $FAPbI_3$ thin films.[27]
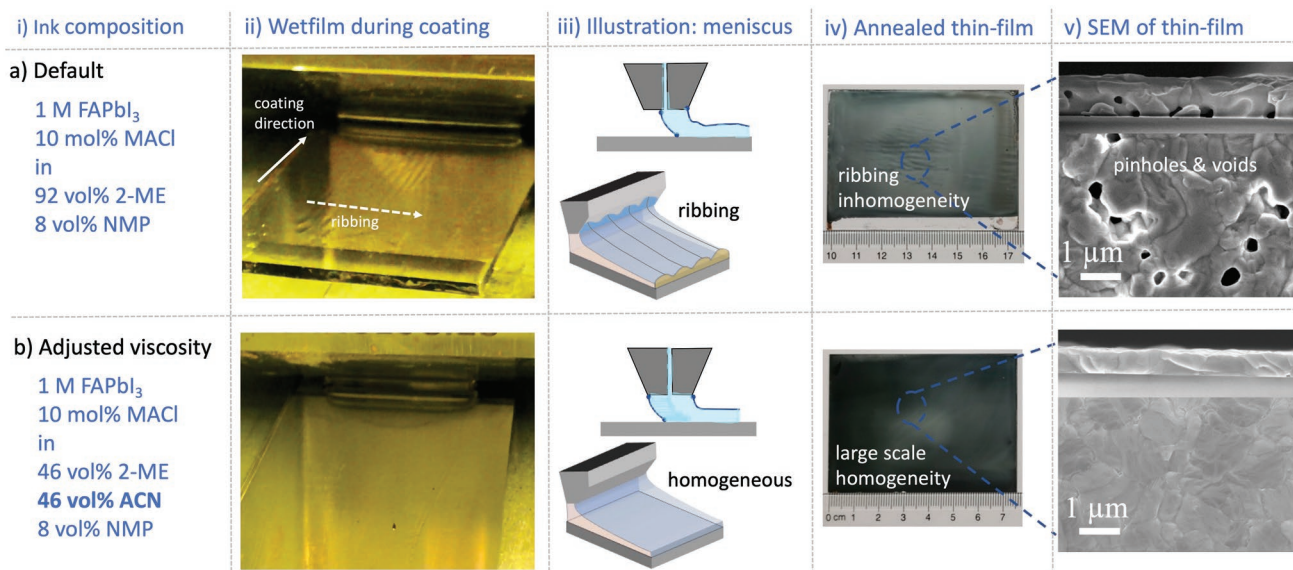
In this work, we, therefore, comment on and distinguish the probable role of different solvent components in precursor solution both on the macroscopic and microscopic (Sections 2.1–2.3) homogeneity and quality of slot-die coated thin films, which directly affects the solar cell performance (Sections 2.4 and 2.5). Optimized inks were used to demonstrate also larger area slot-die coated minimodules reaching 17% PCE on a 12.7 cm^2 active area and we evaluated the long-term stability (Section 2.6) of samples processed from optimized inks compared to the reference ink clearly establishing the detrimental effect of non-ideal thin-film quality due to non-optimal inks and growth also on the long-term performance. We demonstrate the substantial influence of the precursor solution ink composition on the coating homogeneity. $FAPbI_3$ precursor inks based on 2-ME and NMP exhibit ribbing coating inhomogeneities due to non-ideal ink viscosity. With increasing amounts of the co-solvent acetonitrile, ACN, the overall ink viscosity can be reduced to reduce ribbing effects in coated wet films. In this work, we found that for an optimized ACN content of 46 vol% a certified steady-state PCE of 22.3% could be achieved in small-area devices. For mini-modules with active areas of 12.7 cm^2, a device with a champion PCE of 17.1% was achieved. In the meantime, we conducted a full year of outdoor stability tests on encapsulated test-cell devices. They exhibited excellent stability operating without significant performance loss during >9 months of outdoor exposure in the cold days of the year (October–June in Berlin, Germany). After that, from

July to September, it is noted that the average performance of devices slightly decreases during the warmer summer period, which was rationalized by an increased device aging at higher operating temperatures. This work highlights the importance of rational ink design to reduce the ribbing effect enabling large-area slot-die-coated perovskite module technology and we demonstrate the technological potential of PSC prototypes under real outdoor-operating conditions.

2. Results and Discussion

2.1. Ribbing: Large-Scale Coating Inhomogeneity

When coating the precursor ink of $FAPbI_3$ in 2-ME and N-Methyl-2-pyrrolidone (NMP, referred to herein as the 0% ACN "reference" ink), we observed thickness inhomogeneities in the coated wet films by the naked eye, shown in the photographic image in **Figure 2**a. The periodic height variations in the wet-film thickness is a phenomenon referred to as "ribbing", which occurs when the positive pressure gradients and surface tension forces acting on the meniscus during slot-die coating are unbalanced.[12] Ribbing originates from inhomogeneous flow and may persist even the final coating result if coated wet films cannot self-equilibrate to a homogeneous wet film prior to solidifying.[28] In our case, we observed the layer inhomogeneity caused by ribbing to persist and cause inhomogeneity effects in coated perovskite thin films after annealing, as illustrated in the photo of a slot-die coated larger-area sample shown in Figure 2c. From profilometry measurements of the 0% ACN thin-film sample (Figure S1, Supporting Information), we determined the average film-thickness in regions with minimal ribbing effects to be around 853 +/− 40 nm, while the average layer thickness and variation in regions with strong ribbing effects were determined to be around 1415 +/− 170 nm,

i) Ink composition	ii) Wetfilm during coating	iii) Illustration: meniscus	iv) Annealed thin-film	v) SEM of thin-film
a) Default 1 M FAPbI$_3$ 10 mol% MACl in 92 vol% 2-ME 8 vol% NMP	coating direction / ribbing	ribbing	ribbing inhomogeneity	pinholes & voids / 1 µm
b) Adjusted viscosity 1 M FAPbI$_3$ 10 mol% MACl in 46 vol% 2-ME **46 vol% ACN** 8 vol% NMP		homogeneous	large scale homogeneity	1 µm

Figure 2. Comparison of thin-film layer homogeneity for two different precursor inks (i) a) 0% ACN and b) 2-ME/ACN mixed (46% ACN) inks. Images in (ii) show the as-coated wet perovskite thin films while in (iii), sketches of the meniscus and resulting ribbing phenomena are illustrated. Images of the annealed thin films are shown in column (iv) and corresponding SEM top and cross-sectional view of images of perovskite thin films after annealing are shown in column (v).

**ADVANCED
SCIENCE NEWS**

www.advancedsciencenews.com

**ADVANCED
ENERGY
MATERIALS**

www.advenergymat.de

measured perpendicular to the coating direction. This means, that the layer thickness variation is almost double for regions in samples exhibiting ribbing effects.

In addition to a variation in the layer thickness and coating homogeneity, we observed that samples, which show macroscopic ribbing effects also exhibit substantial microscopic layer inhomogeneities. From SEM top-view and cross-section analysis we clearly observe thin films consisting of multiple grains throughout the cross-section with pinholes and voids, as shown in Figure 2a-v). This layer inhomogeneity might originate from differences in local film formation kinetics due to height variations in the wet film (Figure S1, Supporting Information) as well as differences in the relative solvent evaporation rate of the co-solvents.

Ribbing effects can be circumvented by letting wet films equilibrate for a longer time after coating. This is, however, detrimental in the case of halide perovskite coating as solvents need to be rapidly removed to avoid the formation of solvate intermediate phases that may negatively affect the thin-film morphology and microstructure, as discussed in Section 2.3. Another approach to preventing ribbing is to reduce the ink viscosity (Note S2, Supporting Information),[29] we adjusted the precursor ink rheological properties by utilizing the low-viscosity solvent ACN as a co-solvent as discussed in detail in the next section. Figure 2b shows a photographic image of a wet film taken during slot-die coating of the FAPbI$_3$ precursor ink with 46 vol% of ACN (referred to here as 46% ACN ink) as a co-solvent. There are evidently no visible ribbing effects during coating. After gas quenching and annealing, the thin films appeared homogeneous. From SEM images, we observe thin films prepared from inks with optimized ACN content to be pinhole-free and have a morphology with large grains as shown in Figure 2b-v). It can be anticipated that charge carrier transports in such thin films are substantially more efficient compared to thin films with discontinuous grains, as we observed in solar cell devices (see Section 2.5). What becomes apparent from the comparison of the coating homogeneity and thin-film morphology for the inks compared in Figure 2 is that slight changes to the ink composition have dramatic effects on the resulting thin-film morphology.

2.2. Ink Rheology and Layer Homogeneity

To analyze the ink rheology of 2-ME/ACN inks, we performed systematic dynamic viscosity (μ) and surface tension (σ) measurements. Compared to 2-ME with a μ of 1.99 cP, the pure solvent ACN has a very low μ of only 0.34 cP.[30,31] We systematically investigated the rheological properties of FAPbI$_3$ precursor inks with varying fractions of the ACN co-solvent: 0 vol%, 17 vol%, 33 vol%, 46 vol%, and 59 vol% (Figure S2, Supporting Information). Experimental values are shown in Table S1, Supporting Information. As expected, the dynamic viscosity of the perovskite precursor solution is higher compared to the pure solvents. With increasing amounts of ACN from 0% to 59%, the μ of perovskite inks exhibit a close-to linear decrease from 6.67 to 2.07 cP at room temperature, proving that adding ACN with a six times lower μ compared to 2-ME solvent indeed reduces the viscosity of precursor solution.[30,31] The σ of the investigated inks stays at the same level, only slightly decreasing from 32.25 to 30.89 mN/m with the addition of ACN. Both a lower μ and a higher σ of the ink can contribute to avoiding the ribbing effect.[18] In this case, the reduced μ upon addition of ACN to precursor inks promote the leveling of uneven wet films after deposition and hence reduces the ribbing effect of the coated wet films.

To investigate the effect of layer and morphological inhomogeneity caused by ribbing on the optical properties of thin-films samples, we conducted photoluminescence (PL) hyperspectral imaging of corresponding perovskite thin-films (**Figure 3**a). The non-uniform thickness distribution of the thin-film perpendicular to the direction of the deposition caused by ribbing
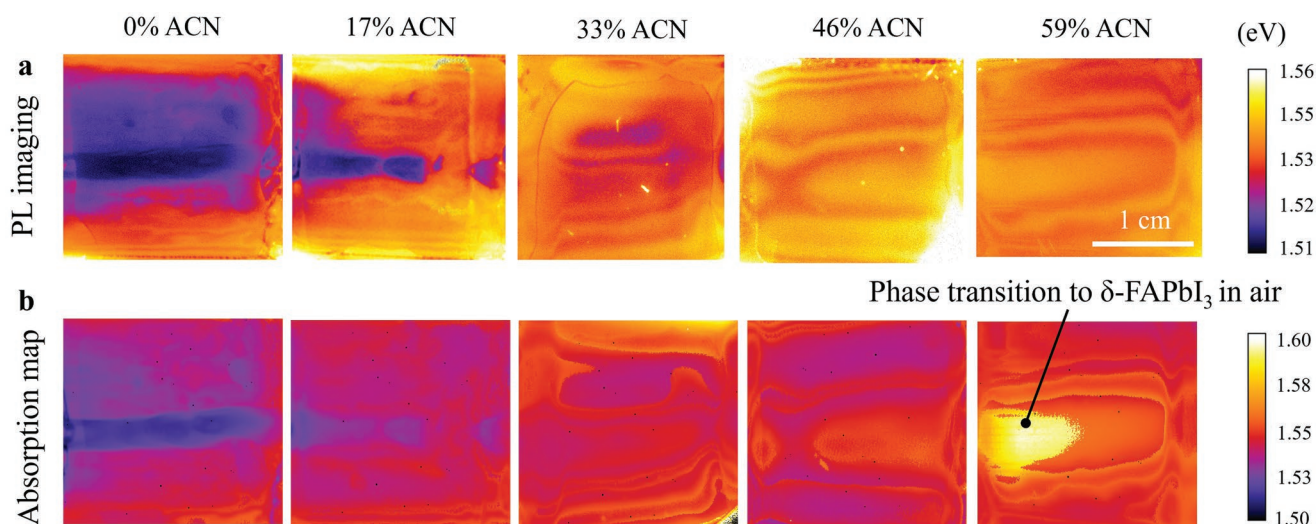
Figure 3. a) The photoluminescence (PL) peak position images of perovskite thin films. b) Absorption energy onset map obtained as a result of fitting a Gaussian peak to the first-order derivative of one minus transmittance as a function of the photon energy of the perovskite thin films. Measurements were carried out on encapsulated samples in the air. Note, the bright spot in the absorption map of the 59% ACN sample. We hypothesized that the increase in apparent bandgap is caused by the onset of the phase transition due to local encapsulation failure.

is apparent in the distribution of the photon energy of the maximum intensity of the PL peak, which we refer to as the PL peak position. For regions with a thicker thin-film thickness, the PL peak position is red-shifted compared to regions with thinner films. To clarify, we calculated the absorptivity for film thicknesses ranging from 100 to 2000 nm (Figure S3, Supporting Information). Meantime, we performed ellipsometry measurements of bare $FAPbI_3$ film (with 0.1 mmol MACl in precursor ink) and derived the absorption and extinction coefficient data, as shown in Figure S4, Supporting Information. Then, we derived the thickness dependence of the PL spectra $\phi_{PL}(E)$ as shown in Figure S3, Supporting Information, in which we show normalized intensity for clarity. From the calculation, the position of the PL peak shifts to lower energy as the thickness of perovskite increases, which is consistent with our observation. In hyperspectral transmittance imaging measurements performed with a white light source (Figure 3b), the locally measured absorption onset shows a similar trend. The variation in the detected PL peak position is in agreement with the film thickness variation as determined by profilometry (Figure S1, Supporting Information). Note, that the PL images and absorption maps were carried out on samples encapsulated with a cover glass with glue encapsulant around the sample edges. Measurements were carried out with a few days in between. We hypothesize that the area of higher bandgap observable in the absorption map for the 59% ACN sample is due to an onset of the phase transition to the $FAPbI_3$ delta phase, which we find can be triggered by ambient humidity. In comparison, perovskite thin films processed from ACN-containing inks exhibit a minimal variation in the PL peak position and absorption energy onset, illustrated by the comparison of the PL peak maximum values as a function of vertical position in Figure S5, Supporting Information. These experimental results confirm that the modification of ink rheology by the addition of a low-viscosity solvent, here ACN, is a viable strategy to improve the thin-film layer homogeneity when slot-die coating halide perovskites. In principle,

The results shown here also demonstrate the applicability of contactless optical PL imaging and absorption maps to determine the thickness homogeneity of thin-film absorber samples such as halide perovskites. As these are non-destructive methods, they can feasibly be implemented as check-ups for layer quality in-between processing steps and probably even as in-line metrology tools in production lines.

2.3. Thin-Film Morphology and Micro-Structure

Apart from causing macroscopic layer inhomogeneities, we also found that areas exhibiting pronounced ribbing inhomogeneities had a more porous and inhomogeneous morphology in dried thin films. This is apparent in scanning electron microscopy (SEM) top-view images and from atomic force microscopy (AFM) measurements, as shown in Figures S6 and S7a, Supporting Information. The porosity of thin films was determined from SEM images and is compared for thin films coated from precursor inks with varying amounts of ACN in **Figure 4**a along with the surface roughness (RMS) determined from AFM measurements. This data shows that perovskite thin films processed from precursor inks with low ACN content, in particular the 0 vol% case, show the highest porosity and surface roughness. Perovskite thin films coated with an ACN content of > 33 vol% exhibited a pinhole-free morphology and relatively low roughness. As shown in Figure 4b, the introduction of ACN enabled reducing the ribbing effect and led to smooth thin films with slightly smaller grains (Figures S8 and S9,
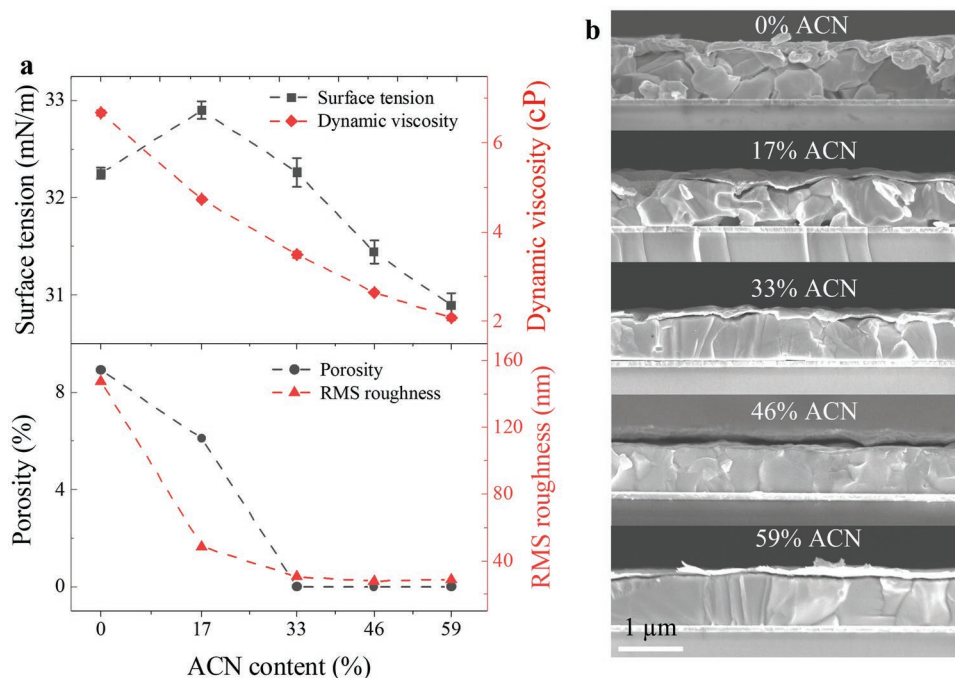
Figure 4. a) The surface tension and dynamic viscosity of perovskite inks versus ACN contents. b) the porosity and surface root-mean-square (RMS) roughness of perovskite thin films fabricated through various amounts of ACN inks.

**ADVANCED
SCIENCE NEWS**

www.advancedsciencenews.com

**ADVANCED
ENERGY
MATERIALS**

www.advenergymat.de

Supporting Information). For high amounts of the ACN co-solvent in the precursor ink (59 vol%), edge defects are observed in the coated perovskite thin films (Figure S8, Supporting Information), which we ascribe to a too rapid solvent evaporation rate due to the low boiling point of ACN. Evidently, reducing the ink viscosity to reduce ribbing effects also beneficially affects the perovskite thin-film morphology, reducing porosity and thickness variation as evidenced in Figure 2.

To investigate any potential influence of the ink composition and growth conditions on the crystal orientation and crystallinity of $FAPbI_3$ thin films, we performed ex situ grazing-incidence wide-angle X-ray scattering (GIWAXS) at the mySpot Beamline.[32] The integrated GIWAXS patterns, shown in Figures S9 and S10, Supporting Information, suggest comparable crystallinity between samples and fairly random crystal orientation with a slight preference for an out-of-plane crystal orientation judged from the 100 α-$FAPbI_3$ reflections. The comparison of the full width at half maximum (FWHM) of XRD peaks suggests that the crystal domain size decreases with ACN addition (Figure S9h, Supporting Information). These results show that, despite the macroscopic layer inhomogeneity due to ribbing effects, the microscopic crystallinity of thin films is comparable.

To confirm that, we mapped the 0% ACN and 46% ACN perovskite thin-film sample with a micron-focus beam of 10 × 100 µm² size, as shown in Figure S11, Supporting Information. The intensity and lattice parameters at 100 α-$FAPbI_3$ reflections of all mapped areas are comparable, indicating that the composition of thin films is homogeneous, which supports the above conclusion.

As solvents may also strongly influence the micro-structure of thin film by directly affecting the growth kinetics and mechanism (stage III in Figure 1), we performed in situ GIWAXS measurements on the precursor inks during drying for varying ACN content (Figure S12 and Note S3, Supporting Information). Note, that these "drying experiments" do not 1:1 match the experimental conditions during slot-die coating deposition of the thin films from the different precursor inks as we utilized an N_2 gas stream from an air-blade to facilitate solvent removal in the latter. We found, however, the experimental data provided valuable insight into the difference in the solvent removal kinetics as well as subtle changes in intermediate crystalline phase forming. Based on the temporal evolution of all diffraction peaks (Figures S13–S15, Supporting Information), we conclude that inks with increasing ACN content exhibit an earlier onset of the intermediate solvate phases' formation. This is consistent with the lower boiling point of ACN (82 °C compared to 124 °C of 2-ME and 202 °C of NMP) evaporating more rapidly leading to the precursor solution reaching solubility limits of perovskite precursor and solvent phases faster.[33] Upon the addition of ACN, we did not observe any additional or particular diffraction peaks that would suggest the formation of solvate phases related to this solvent being incorporated or interacting strongly with the other precursor compounds during film formation. This agrees with ACN having been previously reported to be a weakly coordinating solvent to the lead-halide solution complexes.[33] This is also in agreement with a previous study postulating a direct relationship between the solution-phase lead-halide complex coordination strength of solvents and the formation of solvent-containing crystalline

intermediate phases.[34] We hence propose that the ACN addition affects the thin film morphology and homogeneity by altering the rheological properties of precursor inks and by providing more ideal crystallization conditions as the lower boiling point solvent is more efficiently removed. Note, that GIWAXS measurements were carried out under static drying conditions and the use of an air blade substantially promotes solvent removal.

2.4. Slot-Die Coated Small-Area Test Devices

We investigated the effect of the co-solvent composition and resulting macroscopic and microscopic (see Sections 2.2 and 2.3) layer homogeneity differences on the performance of small-area solar cell devices. Devices were of a p-i-n perovskite solar device configuration. "p" refers to a p-type selective contact layer – in our case, a self-assembled monolayer of (2-(3,6-dimethoxy-9H-carbazol-9-yl)ethyl)phosphonic acid, referred to as MeO-2PACz.[35] "i" refers to the perovskite absorber layer, assumed to be intrinsic. "n" refers to an n-type selective contact, comprised of a triple layer of evaporated layers of lithium fluoride, LiF, fullerene, C_{60}, and bathocuproine, BCP. Copper was used as a back contact material. The device layer stack was hence: Glass | ITO | MeO-2PACz | $FAPbI_3$ (≈750 nm) | LiF (1 nm) | C_{60} (23 nm) | BCP (8 nm) | Cu (100 nm). Prior to the investigation of the 2-ME/ACN co-solvent composition, we also carried out a test series varying the NMP solvent and MACl additive content in precursor inks (see Note S4, Supporting Information) determining the amount of 8 vol% NMP to be ideal.

Figure 5a compares the current density–voltage (J–V) curves of representative small-area test devices made from precursor solutions with varying co-solvent content. The average and maximum device performance show a systematic trend with champion performance up to 21.3% achieved for devices made from the 46% ACN precursor solution. We summarize the photovoltaic parameters of PSCs in Table S2 and Figure S16, Supporting Information, respectively. Comparing the steady-state output of devices manufactured from inks with 0 vol%, 17 vol%, 33 vol%, 46 vol%, and 59 vol% ACN, average PCE values of 13.7%, 16,7%, 19.6%, 20.7%, and 18.7% are observed over a measurement-time of 180 s (Figure 5). We find a direct correlation between the improved thin-film quality discussed in Section 2.3 and the solar cell device performance with cells made from inks with >33 vol% ACN exhibiting dramatically improved photovoltaic performance (V_{OC}, J_{SC}, FF, and PCE) as shown in Figure 4c. Improving the thin-film layer homogeneity and reducing pinholes in dried thin films enable superior thin-film quality, which is also reflected in the trend for the device performance.

Visible in the J–V curves shown in Figure 5, the hysteresis between forward and reverse measurement directions is affected by the precursor ink co-solvent composition as well. To analyze the J–V discrepancy further, we carried out transient analysis during maximum power point tracking (TrAMPPT), which we have established as a tool to quantify the current response of solar cells upon voltage perturbation close to the maximum power point[36,37] shown in Figures S17–19,
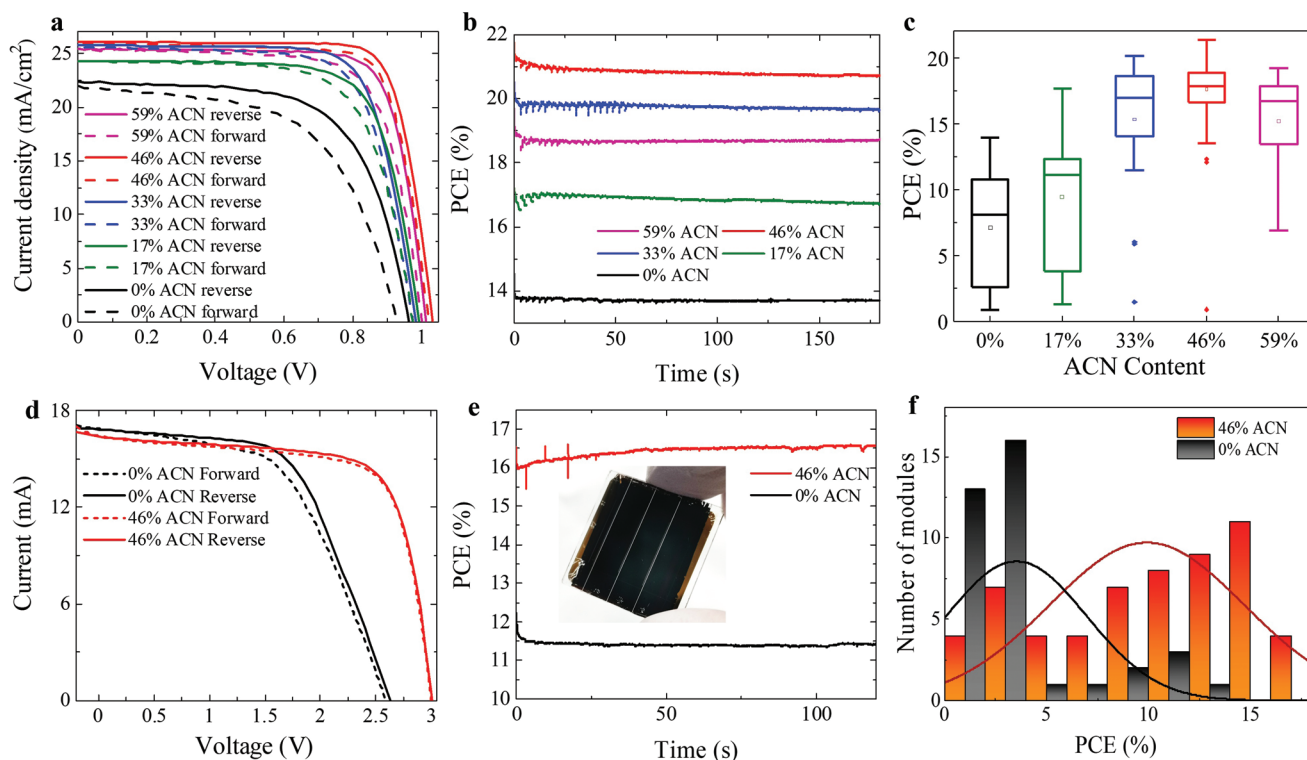
Figure 5. Photovoltaic performance of small-area test devices (6 × 0.2 cm² pixels on 1 square inch substrates) and "micro"-modules (three 5 mm subcells on 1 square-inch substrates, shown in the inset of(e)) of slot-die coated PSCs. a) the current density–voltage (J–V) curves and b) the stabilized output at the maximum power point tracking data of champion devices slot-die-coated from precursor inks with different ACN content. c) PCE histograms of all devices. d) the J–V curves of "micro"-modules (active area of 2.2 cm²), e) the stabilized output at the maximum power point (MPP), and f) histogram plots of the mini-modules made from precursor inks containing 0% and 46% ACN.

Supporting Information. Compared to devices fabricated from 0% ACN precursor inks, the devices made with 46 vol% ACN exhibit a dramatic reduction of the amplitude of current transients with respect to the steady-state current density extracted from the devices. This can be directly linked to the differences in the perovskite absorber layer micro-structure as charge-carrier transport in-between grains causes additional capacitive effects and a sluggish current collection. As evident from the SEM shown in Figure 2b-v, samples made from 0 vol% ACN precursor solutions exhibit more meso-crystalline morphologies with many inter-grain boundaries in the direction of charge carrier transport while the thin-film samples made from 46 vol% ACN precursor solutions appear very homogeneous with large grains and negligible grain boundaries observable in the vertical direction. The more inhibited charge carrier transport in the samples with multiple grain boundaries in the direction of charge carrier transport in the solar cell device is directly reflected in the more sluggish transient response of the photocurrent and overall lower charge carrier density measured for devices made from 0 vol% ACN precursor solutions.

Losses in device performance due to a low absorber layer quality become even more apparent when scaling devices to larger areas. To illustrate this fact, we fabricated micro-modules for precursor inks with no (0 vol% ACN) and the optimized amount (46 vol% ACN) of ACN. Corresponding J–V curves of micro-modules with three sub-cells on square-inch substrates and a total active area of 2.2 cm² are shown in Figure 5d–f. The

laser scribing techniques were used to pattern the layer stack in individual sub-cells.[38] Obviously, the device performance of micro-modules processed from 0 vol% ACN precursor inks is substantially lower due to a significantly lower fill factor that can be attributed to a higher series resistance in the device layer stack (Figure 5d). This is also reflected in the substantially lower steady-state performance (Figure 5e) of devices compared to devices processed with 46 vol% ACN and a lower average performance as shown in the histograms of Figure 5f (see Note S5, Supporting Information).

2.5. Optimized Device Architecture and Mini-Modules

After achieving high device performance with the 46 vol% ACN precursor ink on smaller area test devices and micro-modules (2.2 cm² active area), we carried out further optimization of the solar cell device architecture and selective contact layers to maximize the device performance. We utilized an alternative molecular self-assembled layer of Me-4PACz ((4-(3,6- dimethyl-9H-carbazol-9-yl)butyl)phosphonic acid) as a hole transport layer (HTL). This was motivated by a higher hole-extraction efficiency and lower interfacial losses at the interface between the self-assembled monolayer and the perovskite layer, as recently demonstrated in higher bandgap perovskite single junction and tandem solar cells.[39] Also, we utilized an ALD-deposited layer of tin oxide, SnO_2, instead of BCP when manufacturing

ADVANCED
SCIENCE NEWS
www.advancedsciencenews.com

ADVANCED
ENERGY
MATERIALS
www.advenergymat.de
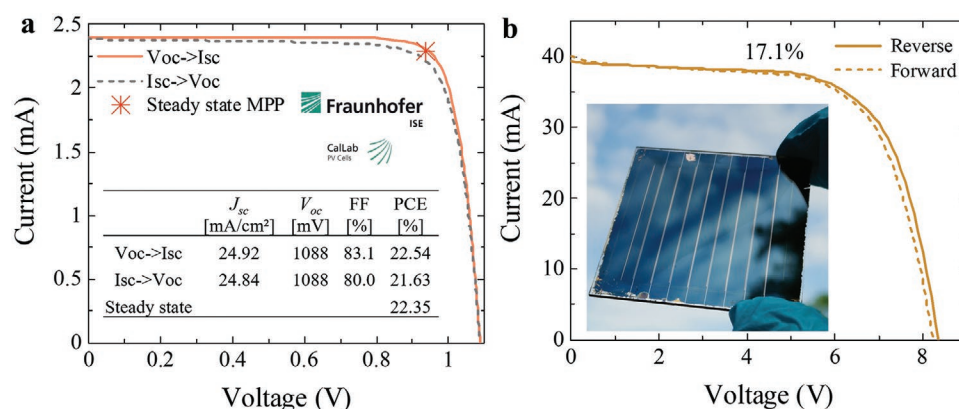
Figure 6. Champion photovoltaic performance of slot-die coated small area and mini-modules PSCs. a) the *J–V* curves of the best device with Me-4PACz as HTL. The cell was measured and certified in Fraunhofer ISE CalLab. The inserted table includes photovoltaic parameters. b) *J–V* curves of a 5 by 5 cm mini-module. The insert is a corresponding optical image.

mini-modules and samples for long-term performance evaluation discussed in Section 2.6, as BCP is introducing lower longer-term stability.[41] The layer stack was hence: Glass | ITO | Me-4PACz | FAPbI$_3$ ($\approx$750 nm) | LiF (1 nm) | C$_{60}$ (23 nm) | SnO$_2$ (20 nm) | Cu (100 nm). Note, that the replacement of BCP with SnO$_2$ provides similar device performance, as shown in Figure S30, Supporting Information. As the deposition of SnO$_2$ requires separate deposition steps and is far more time-consuming than BCP, the latter is utilized for high-throughput device performance screening while SnO$_2$ is only used when the device's long-term performance is of high relevance.

With these modifications, we were able to push device performances even higher and reached a champion device efficiency of 22.54%, certified by Fraunhofer ISE CalLab, with V_{OC} of 1.088 V, FF of 83.1%, a J_{SC} of 24.9 mA cm^2 and a steady state PCE of 22.35%, as illustrated in **Figure 6** and Figures S20–22, Supporting Information. To our knowledge, this is the highest certified PCE achieved from slot-die-coated perovskite solar cells and among the highest values achieved for inverted PSCs irrespective of the perovskite absorber deposition procedure. The external quantum efficiency (EQE) of the champion device was measured as well (Figure S23, Supporting Information), giving an integrated J_{SC} of 24.67 mA cm^{-2}; the dfference is less than 2% compared to the value obtained from *J–V* curves, which is acceptable. The band gap of the champion PSC calculated from the derivative of the EQE curve is 1.519 eV (Figure S23, Supporting Information).

In the next step and taking advantage of the optimized precursor ink as well as improvements in the device layer stack described for the optimized and certified devices, we also fabricated mini-modules on substrates of 5 × 5 cm^2 with eight series-interconnected sub-cells. We were able to obtain a champion PCE of 17.1% in reverse scan with a V_{OC} of 8.36 V, a FF of 66.8%, and a J_{SC} of 3.06 mA cm^2 for a total active area of 12.7 cm^2 (Figure 6b and Table S3, Supporting Information). To compare the current density generated per sub-cell in modules with the current density obtained for pixel devices, we estimated the sub-cell current density by dividing the module current measured with the sub-cell area of 1.58 cm^2, which is 24.4 mA cm^{-2}. This result highlights that, in terms of photo-current, losses between small-area test cells and modules are fairly negligible

indicating a high degree of absorber layer homogeneity and optoelectronic quality. This result is a fairly high-performance demonstration for a perovskite module of medium size and demonstrates the importance of optimizing ink formulation and process conditions to enable high-quality large-area coatings (see Note S5, Supporting Information). Losses in device performance predominantly stem from a lower V_{OC}, and FF compared to the small-area test devices, which will need to be reduced by decreasing series resistance and shunt resistance losses as well as recombination, which is expectedly high in the interconnect region of modules, where layer damage due to the laser ablation process and direct contact between metal top contact and perovskite absorber layers are expected.

2.6. Long-Term Operational Stability

Representative devices manufactured with 46 vol% ACN co-solvent content in precursor solutions, were measured with maximum power point (MPP) tracking over 12 h (Figure S24, Supporting Information). The PCE decreased at the first hour and then slowly increased to a stable PCE level at around 20%, indicating that the device exhibits almost no degradation but some slow photo-induced processes within this time frame. Continuous illumination stress tests (ISOS-L-1I) were carried out in a custom-built high-throughput aging setup for devices manufactured with 0 vol% and 46 vol% ACN in the precursor solutions.[40] For stability tests, the BCP layer was replaced with a SnO$_2$ buffer layer (Table S4, Supporting Information) as this has been shown to provide substantially better long-term stability.[41] All those cells show an increasing PCE at the initial stage and reach the maximum efficiencies after 30 h, which could be rationalized as a strong light-soaking phenomenon, as illustrated in **Figure 7**a.[42] The 0% ACN cells exhibit fast degradation after 160 h of tracking and maintained $\approx$47% of their maximum efficiency after 250 h, which is probably due to the porous morphology of perovskite thin films. However, the 46% ACN samples maintained over 89% of their maximum PCEs after 250 h of continuous MPP tracking and exhibited an estimated T_{S80} of 453 h (Figure S25, Supporting Information), where T_{S80} is the time required to approach 80% of their

**ADVANCED
SCIENCE NEWS**

www.advancedsciencenews.com

**ADVANCED
ENERGY
MATERIALS**

www.advenergymat.de
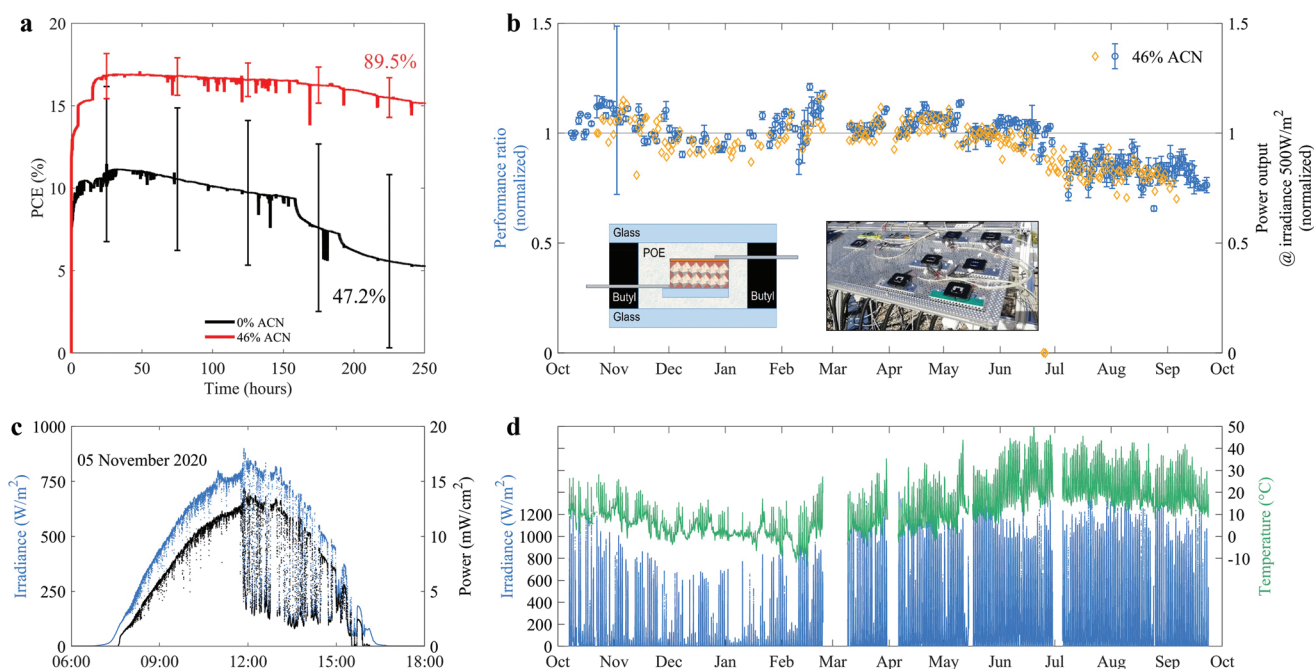
Figure 7. Indoor and outdoor aging of slot-die-coated FAPbI₃ PSCs a) The indoor long-term MPP tracking of small area 0% ACN (average from 7 PSCs) and 46% ACN (average from 14 PSCs) devices under continuous one sun illumination at 25 °C tracked in nitrogen atmosphere (ISOS-L-1I). b) Time evolution of normalized performance ratio (averaged over three PSCs) and cell MPP power at 500 W m⁻² during the outdoor exposure (ISOS-O-2) for small area devices with 46% ACN. The inserted photographs are the devices fixed outdoors in an open rack configuration and schematics of device encapsulation. c) Changes in the global irradiance in the plane of array and PSC power output during one day. d) Device temperature and global irradiance during the entire period of exposure (The loss of datasets is due to technical difficulties with the monitoring setup. During those periods, cells were still exposed outdoors continuously without MPP tracking).

maximum PCE.[43] Integral lifetime energy yield (LEY) was used to estimate the cell's ability to generate power over time,[44] as shown in Figure S26, Supporting Information. The LEY of devices made from 46 vol% ACN in precursor inks is almost twice compared to 0 vol% ACN devices.

Optimized devices with SnO₂ interlayer were exposed to outdoor conditions to trace their operational stability under real-world conditions (Table S4, Supporting Information). For this, the devices were encapsulated between two glasses using poly-olefin (POE) as an encapsulant and butyl rubber as the edge sealant (Figure 7b) to prevent moisture- and oxygen-induced degradation. Figure 7b summarizes the details of PSCs' power output recorded in the period from October 2020 to September 2021 in Berlin and the corresponding weather conditions. These testing conditions can be systematically categorized to follow the ISOS-O-2 protocol.[43] In Figure 7c, we use time evolutions of normalized performance ratio and cell power output at an irradiance of 500 W m⁻² (see Experimental Section for details) to illustrate cells' outdoor stability. During this time, the cells were placed on the fixed tilted stand on the rooftop and connected to maximum power point trackers. Similar to the dozens of hours of indoor exposure, the devices' performance slightly improved during the first month of outdoor exposure. Further changes reflect seasonal changes in the weather conditions until summer starts when a pronounced systematic decrease in performance was registered. While further studies are required to decouple seasonal changes from permanent degradation effects. In the beginning, the device

performance throughout the ≈9 months of outdoor operation was fairly constant and device performance loss negligible. Such impressive outdoor stability is unexpected considering the indoor stability results measured under continuous illumination (Figure 7a). We believe that day/night cycling allows for sufficient recovery in the device under investigation during the dark period resulting in a substantially prolonged operational lifetime. Reversibility of degradation effects has been previously demonstrated in different PSCs.[45] Figure S27, Supporting Information shows several light/dark cycles in one of our cells demonstrating strong reversible processes that undoubtedly contribute to the device's outdoor operation. We believe that cloudy days, as well as day/night cycling, enable sufficient recovery of device performance, which seems to dramatically improve the measured device lifetime compared to the continuous illumination experiments described above (ISOS-L-1I).[46] The slow continuous decrease in device performance indicates non-reversible degradation mechanisms taking place during summer months when temperatures increase (July–September, Berlin). Assuming an approximately linear decrease in performance ratio during this period of time, a degradation rate of ≈0.1% per day is observed. We hypothesize that the origin of such a decrease might be a more rapid illumination-induced degradation at higher device temperatures (Figure 7d). To confirm this, we performed a long-term indoor MPP tracking of 46% of devices at 85 °C (ISOS-L-2I) as shown in Figure S28, Supporting Information. It is clearly observed that the average performance of devices rapidly degrades until 35% of their

**ADVANCED
SCIENCE NEWS**

www.advancedsciencenews.com

**ADVANCED
ENERGY
MATERIALS**

www.advenergymat.de

initial PCE after 1000 h of continuous tracking. After the stability test, X-ray diffraction (XRD) experiments were carried out on one of the aged devices with results shown in Figure S28, Supporting Information. The crystallographic features were comparable to the sample prior to degradation studies suggesting that the perovskite absorber layer remains fairly intact and performance decay is likely related to interfacial degradation between the perovskite absorber and the charge-selective contact layers. We acknowledge that stress factors other than light and temperature could also cause degradation during the summer period, most importantly the humidity ingress through the encapsulation. To test this, we performed a long-term damp-heat test on our encapsulated devices (Figure S29, Supporting Information), for which the cells were placed into the chamber with 85% relative humidity and 85 °C (ISOS-D-3). Only a marginal decrease of ≈15% on average was observed after 1000 h strongly suggesting that the encapsulation provides significant moisture barrier properties (when this is not the case, we observe visible changes due to perovskite decomposition and rapid decrease in PCE). The decrease in PCE in this experiment, and therefore in the summer period of the outdoor experiment, is again related to the device's thermal stability and has a similar mechanism of interfacial degradation as described above. More detailed work is needed to disentangle the intrinsic degradation of the perovskite absorber from device performance losses due to interfacial or contact-layer degradation in order to design appropriate technical solutions to improve the long-term stability of PSCs. In addition, detailed studies to investigate the effect of temperature as a potential accelerating factor in solar cell device degradation needs to be carried out.

Our results represent one of the few full-season assessments of a perovskite device's performance under real-condition outdoor conditions. This is the first full year of an outdoor performance test carried out on FAPbI$_3$-based solar cells manufactured with scalable deposition methods but experiments with shorter duration have been carried out prior.[47] Our results illustrate, that full-seasonal testing is crucial as the concerted effects of varying levels of irradiation as well as temperature play a major role in device degradation. For a reliable assertion and prediction of the long-term performance of perovskite solar cells, the influence of multiple degradative factors has to be considered.

3. Conclusion

When scaling MHP absorber layer deposition to larger areas, precursor inks and process parameters need to be re-engineered to enable high-quality material coatings and high-performance devices. We here highlight that the rheological properties of the precursor inks are a determining factor for the larger-scale homogeneity of coated thin films. We show that tuning the precursor ink viscosity by adding the low-viscosity co-solvent acetonitrile to 2-ME-based FAPbI$_3$ precursor inks enabled us to avoid ribbing effects that cause layer thickness inhomogeneities and unfavorable thin-film microstructure. We systematically analyzed the role of ACN in the ink on sample coating homogeneity composition and morphology. In situ GIWAXS experiments provided further evidence that also the solvent removal and crystallization kinetics changed when replacing 2-ME with

the lower boiling point solvent ACN. More experimental work is needed to deconvolute the different roles solvent play during the various stages of thin-film processing illustrated in Figure 1.

At an optimized amount of 46% volume of ACN, we demonstrated slot-die-coated perovskite solar cell devices with a certified power conversion efficiency of 22.3%, which is the highest certified value for a slot-die-coated perovskite solar cell. To emphasize the importance of ink optimization to achieve high-quality large-area coatings we also demonstrated series-interconnected mini-modules with PCEs of > 17% on > 12 cm^2 active areas. In addition to demonstrating excellent scalability of precursor ink system and devices architecture, we also carried out indoor stress tests (1000 h at ISOS-L-2I conditions and 250 h at ISOS-L-1I conditions) and outdoor operational stability tests (≈12 months at ISOS-O-2) on the slot-die-coated FAPbI$_3$ devices. We report only marginal degradation under outdoor operational conditions for over 9 months when the device performance even benefited from day-night cycling. However, we demonstrated that temperature is a key factor in accelerating degradation as devices slowly decay during the hot summer season. This work covers a wide range of aspects of importance for the further development of PSCs: from fundamental insight into the role of different components in precursor inks in the formation of high-quality thin films to scaling device technology to larger device areas and assessing the performance under different long-term exposure conditions.

4. Experimental Section

Materials: Lead (II) Iodide (99.99%, trace metals basis), Self-assembled monolayer [2-(3,6-dimethoxy-9H-carbazol-9-yl)ethyl] phosphonic acid (MeO-2PACz) and [4-(3,6- dimethyl-9H-carbazol-9-yl) butyl]phosphonic acid (Me-4PACz) were purchased from Tokyo Chemical Industry (TCI). Formamidinium iodide (FAI) and methylammonium hydrochloride (MACl) were purchased from Dynamo. Bathocuproine (BCP) was purchased from Ossila. Ethanol (anhydrous) was purchased from VWR Chemicals and copper shots were purchased from Alfa Aesar. Other chemicals were purchased from Sigma-Aldrich. All the chemicals were used as received without purification.

Perovskite Precursor Inks Preparation: For 2-ME ink (0% ACN), 1 mmol FAI, and PbI$_2$ powders were scaled and mixed in a vial and dissolved with 0.92 ml 2-methoxyethanol (2-ME) and 0.08 ml (≈0.83 mmol) N-Methyl-2-pyrrolidone (NMP) solvents, the vial was stirring to dissolve at room temperature. The acetonitrile (ACN) inks were prepared as the same procedure, the solvents are mixed of 19%, 33%, 46%, and 59% volume fraction of ACN with respect to the 2-ME. For example, 1 mL 46% ACN ink was composed of 0.46 ml of ACN and 2-ME as well as 0.08 mL NMP with 461.01 mg (1 mmol) lead iodide and 171.97 mg (1 mmol) PbI$_2$ with 6.75 mg MACl (0.1 mmol).

Fabrication of Perovskite Devices: The stack of PSCs discussed in this work are p-i-n configuration with layer stack: ITO | MeO-2PACz | FAPbI$_3$ (≈750 nm)| LiF (1 nm)| C$_{60}$ (23 nm)| BCP (8 nm)| Cu (100 nm). For the long-term stability test and module fabrication, a device configuration was performed with ITO | MeO-2PACz | FAPbI$_3$ | LiF | C$_{60}$| SnO$_x$ | Cu. For the champion device (the certified device), a device configuration of ITO | Me-4PACz | FAPbI$_3$ | LiF | C$_{60}$ | SnO$_x$ | Cu was conducted. The pre-patterned indium tin oxide conductive substrates (ITO, inch by inch, 15 Ω sq^{-1}, ≈150 nm) were cleaned in the same procedure as described previously.[11] After regular cleaning, the ITO substrates were treated with UV-ozone for 15 min. The MeO-2PACz or Me-4PACz solution (1 mmol) was spin-coated onto the ITO surface at the speed of 3000 rpm for 30 s with 1000 s^{-1} ramping, the substrates were immediately transferred to a pre-heated hot plate at 100 °C for 10 min.

Slot-Die Coating Perovskite Layers: The perovskite thin films were coated by a slot-die coater (FOM technologies) in a nitrogen glovebox with a content of water and oxygen less than 1 ppm. The air knife was mounted on the top of the chuck (≈10 cm height) with ≈20 PSI inner pressure. The perovskite precursor ink was fed into the slot die head with a tubbing connected to the syringe pump system, which can precisely control the pump rate of ink. The coating speed was set at 20 cm min^{-1}, the pump rate as 100 µl min^{-1}, and 0.2–0.3 mm gap at room temperature. After coating, the wet perovskite thin films were immediately treated with dried nitrogen gas through an air knife, which had a pressure of around 20 PSI over its entire length. As treated films were rapidly transferred to a pre-heated hot plate at 150 °C and annealed for 15 to 20 min.

Module Fabrication and Laser Patterning: The perovskite layers were slot die coated using the same procedures as small-area solar cells. The structuring of the samples was carried out by a laser system from Rofin Baasel Lasertech with a picosecond laser source with a pulse peak power of ≈8MW at a pulse duration of about 10 ps. The layout and schematic of the mini-modules could be found in the previous work.[11] To avoid material degradation, the samples were stored in a patterning chamber with constant nitrogen flow. The P1 process was performed using a picosecond laser with a wavelength of 1064 nm, 500 kHz, POD2, fluence of 10.88 J cm^{-2}, and a high pulse overlap (≈90%). Thus, a clean and even ablation of the ITO was achieved without thermally affecting the peripheral areas resulting in high electrical insulation of over 20 MΩ. The P2-patterning was carried out with a picosecond (ps) laser (λ = 532 nm, 10 ps, pulsed at 100 kHz, POD5 and fluence 1.32 J cm^{-2}). Three times patterning with a pulse overlap of about 63% allowed a clean and even trench bottom without damaging the underlying ITO layer with a low amount of PbI$_2$ residuals,[47,48] which was reflected in a small series resistance. For the structuring of the counter electrode (P3-process), ps-pulses, 532 nm with 100 kHz, POD5, speed of 4.11 J cm^{-2} was applied. A small overlap of ≈7% helped to decrease the so-called "flaking" of the counter electrode. By multiple patterning (three times), an even layer removal with stable edges was achieved. The active area of the mini-module and micro-module were 12.7 and 2.2 cm^2, consisting of eight sub-cells with an active area of 1.58 cm^2 and three sub-cells of 0.74 cm^2, respectively.[49]

Evaporate Electron Transport and Contact Layers: After annealing, all the substrates were put into an evaporation system (MBRAUN ProVap 3G). Lif (1 nm), BCP (8 nm), C$_{60}$ (23 nm), and copper (100 nm) were subsequently deposited by a thermal evaporation method. At a base pressure of 1×10^{-6} mbar, the evaporation rate of Lif, BCP, C$_{60}$, and copper was controlled at 0.03, 0.1, 0.05 to 0.1, and 0.1 to 1 Å s^{-1}, respectively. For champion devices, a 100 nm sodium fluoride (NaF) layer was deposited upon the glass side at a base pressure of 1×10^{-6} mbar, with a rate of 0.1–1 Å s^{-1}. The active area of all the PSCs is 0.16 cm^2 (determined by the overlap area of ITO and copper) and a 0.105 cm^2 mask determined by microscope imaging was used to define the active area precisely. For the devices with a tin oxide contact layer, 20 nm of SnO$_2$ was then deposited by thermal ALD in an Arradiance GEMStar reactor instead of a BCP contact layer.[38]

J–V Measurements: The measurement geometries and methodologies were conducted analogously as previously reported.[11] In brief, the solar cells were measured under an AM 1.5G 100 mW cm^{-2} illumination (Oriel LCS-100 class ABB solar simulator) with a silicon reference cell (Fraunhofer ISE) as spectrum and intensity calibration. The J–V scans were conducted from 1.2 to −0.02 V (reverse scan) or −0.02 to 1.2 V (forward scan), with a 30 ms delay time, 40 ms integration time, and 20 mV voltage step at room temperature in an N$_2$-filled glovebox without any precondition. The black aperture mask for the champion device was made of black type. The area was defined by a microscope. For the mini-module, the measurements were performed without masks.

Indoor Stability Tests: Solar cells were aged in a custom-built high-throughput aging setup.[40] The detailed procedure could be found elsewhere.[50] In brief, all solar cells were aged under constant MPP tracking in nitrogen at a temperature of 25 or 85 °C at 1 sun illumination. The test is in accordance with the protocol ISOS-L-1I and ISOS-L-2I.[43]

Outdoor Stability Tests: The outdoor measurement station is located on the roof in Berlin with coordinates 52°25″53.5″ N 13°31′27.7″ E. The investigated samples were placed on a tilted (35°) stand facing South. The irradiance measurements performed by EKO ML-02 Si-pyranometer were recorded every 2 s using Picotech PT-104 datalogger. The cell temperature was measured with the DS18B20 temperature sensors attached to the back side of the encapsulated cells. The cell power output was recorded by MP2005M6 MPP trackers (LPVO), which kept cells at MPP condition using perturb and observe algorithm.

A performance assessment parameter performance ratio (PR) was used. PR was calculated for every day as daily cell output energy divided by daily plane-of-array insolation multiplied by the initial cells' PCE at standard test conditions (STC)

$$\text{PR} = \frac{\int_{00:00}^{23:59} P_{\text{MPP cell}}(t)\,dt}{\text{PCE}_{\text{STC}} * \int_{00:00}^{23:59} P_{\text{irradiance}}(t)\,dt} \quad (1)$$

In the calculation of PR, only days with insolation greater than 0.27 kWh m^{-2} were included. Cell power output at an irradiance of 500 W m^{-2} was calculated for days with sufficient data points in the 500 ± 10 W m^{-2} irradiance range. Both parameters were calculated for three outdoor exposed devices and averaged. The test was in accordance with the protocol ISOS-O-2.

Atomic Force Microscopy (AFM): AFM images were recorded with dimension icon AFM from Bruker (ScanAsyst in Air) with a silicon tip on a nitride lever in tapping mode.

Photoluminescence (PL) and Transmittance Hyperspectral Imaging Measurements: PL and white light transmittance imaging measurements were recorded with a Si CCD camera (Allied Vision) coupled with a liquid crystal tunable filter. For transmittance imaging measurements, the illumination was performed with a fiber-optic light panel (Dolan–Jenner industries) connected to a tungsten–halogen light source (Thorlabs). PL imaging measurements were obtained with 450 nm LED and excitation photon flux was adjusted to 1.7×10^{21} m^{-2} s^{-1}. Micro-manager software was used for automating the measurements.[51]

The PL spectrum of semiconductors follows the relation.[52,53]

$$\phi_{PL}(E) = a(E)\phi_{bb}(E) \cdot \exp[\Delta E_f / (k_B T)] \quad (2)$$

which links the absorptance $a(E)$ (or absorptivity) of a semiconductor to its luminescence spectrum $\phi_{PL}(E)$. Here, ΔE_f is the quasi-Fermi level splitting, k_B is the Boltzmann constant, and $\phi_{bb}(E)$ is the spectrum of a planar black body at a temperature T into a hemisphere which follows:

$$\phi_{bb}(E) = \frac{2\pi E^2}{h^3 c^2} \frac{1}{\left[\exp\left(\frac{E}{kT}\right) - 1\right]} \approx \frac{2\pi E^2}{h^3 c^2} \exp\left(\frac{-E}{kT}\right) \quad (3)$$

Because the absorptance of a semiconductor depends exponentially on the product of the absorption coefficient a times the thickness d of the film $a(E) = (1 - R)(1 - \exp(-\alpha d))$, the influence of thickness on the shape of the PL spectrum was explored.[53]

In Situ GIWAXS Measurements: The perovskite ink was dropped on the glass substrate which was located on the top of an Anton–Paar heating stage. The ink was covered with a dome within 6 L h^{-1} nitrogen flow. The sample was irradiated by X-rays at the KMC-2 beamline[54] at the synchrotron source BESSY II (Helmholtz-Zentrum Berlin). The ex situ GIWAXS and mapping were measured at the mySpot beamline[32] at an incidence angle of 2°, using radiation energy of 9 keV (λ = 1.378 Å). In situ GIWAXS was done at KMC-2 beamline[54] at an incidence angle of 2°, using radiation energy of 8.048 keV (λ = 1.5406 Å, same as Cu-Kalpha1) and an Anton Paar DHS 1100 domed heating stage. The perovskite ink was dropped on the glass substrate placed on the heating stage and covered with a dome within 0.2 L min^{-1} nitrogen flow. An

external thermocouple was used, which was not standard on AP-furnace, to measure the temperature of samples.

Spectroscopic Ellipsometry Measurements: Spectroscopic ellipsometry measurements were carried out with a Sentech SENResearch 4.0 ellipsometer in the wavelength range of 240 to 1040 nm (≈1 nm steps), with incidence angles varying from 50° to 70°, in 5° increments. The sample structure was of a bare perovskite film deposited atop a fused quartz substrate. Care was taken to limit the measurement spot to a homogeneous region of the film, in order to avoid any thickness gradients. Samples were kept in sealed bags and purged with nitrogen until just before measuring, in order to minimize any possible prior degradation. To simplify the fitting procedure, the backside of the substrate was covered with index-matching diffuse tape in order to suppress backside reflections. Fits were performed using seven Tauc–Lorentz oscillators and assuming surface roughness

Supporting Information

Acknowledgements

Conflict of Interest

The authors declare no conflict of interest.

Author Contributions

Data Availability Statement

Keywords

[1] M. M. Lee, J. Teuscher, T. Miyasaka, T. N. Murakami, H. J. Snaith, *Science* **2012**, *338*, 643.

[2] G. Xing, N. Mathews, S. Sun, S. S. Lim, Y. M. Lam, M. Graïzel, S. Mhaisalkar, T. C. Sum, *Science* **2013**, *342*, 344.

[3] D. P. McMeekin, S. Mahesh, N. K. Noel, M. T. Klug, J. Lim, J. H. Warby, J. M. Ball, L. M. Herz, M. B. Johnston, H. J. Snaith, *Joule* **2019**, *3*, 387.

[4] N. Park, K. Zhu, *Nat. Rev. Mater.* **2020**, *5*, 333.

[5] T. J. Jacobsson, A. Hultqvist, A. García-Fernández, A. Anand, A. Al-Ashouri, A. Hagfeldt, A. Crovetto, A. Abate, A. G. Ricciardulli, A. Vijayan, A. Kulkarni, A. Y. Anderson, B. P. Darwich, B. Yang, B. L. Coles, C. A. R. Perini, C. Rehermann, D. Ramirez, D. Fairen-Jimenez, D. Di Girolamo, D. Jia, E. Avila, E. J. Juarez-Perez, F. Baumann, F. Mathies, G. S. A. González, G. Boschloo, G. Nasti, G. Paramasivam, G. Martínez-Denegri, et al., *Nat. Energy* **2022**, *7*, 107.

[6] F. Mathies, E. J. W. List-Kratochvil, E. L. Unger, *Energy Technol.* **2019**, *81*, 1900991.

[7] J. E. Bishop, C. D. Read, J. A. Smith, T. J. Routledge, D. G. Lidzey, *Sci. Rep.* **2020**, *10*, 6610 .

[8] J. Li, H. Cao, X. Wang, H. Zhu, Z. Dong, L. Yang, S. Yin, *ACS Appl. Energy Mater.* **2019**, *2*, 2506.

[9] M. Roß, L. Gil-Escrig, A. Al-Ashouri, P. Tockhorn, M. Jošt, B. Rech, S. Albrecht, *ACS Appl. Mater. Interfaces* **2020**, *12*, 39261.

[10] Y. Deng, C. H. Van Brackle, X. Dai, J. Zhao, B. Chen, J. Huang, *Sci. Adv.* **2019**, *5*, aax7537.

[11] J. Li, J. Dagar, S. Oleksandra, M. A. Flatken, H. Köbler, M. Fenske, C. Schultz, B. Stegemann, J. Just, D. M. Többens, A. Abate, R. Munir, E. Unger, *Adv. Energy Mater.* **2021**, *11*, 2003460.

[12] H. Benkreira, J. B. Ikin, *Chem. Eng. Sci.* **2016**, *150*, 66.

[13] B. Park, O. E. Kwon, S. H. Yun, H. G. Jeon, Y. H. Huh, *J. Mater. Chem. C* **2014**, *2*, 8614.

[14] S. Hong, J. Lee, H. Kang, K. Lee, *Sol. Energy Mater. Sol. Cells* **2013**, *112*, 27.

[15] S. Chen, X. Dai, S. Xu, H. Jiao, L. Zhao, J. Huang, *Science* **2021**, *373*, 902.

[16] I. Zimmermann, M. Al Atem, O. Fournier, S. Bernard, S. Jutteau, L. Lombez, J. Rousset, *Adv. Mater. Interfaces* **2021**, *8*, 2100743.

[17] T. A. L. H. Xiaoyu Ding, J. Liu, *AIChE J.* **2016**, *62*, 2508.

[18] P. M. S. Stephan, F. Kistler, in *Liquid Film Coating: Scientific Principles and Their Technological Implications* (Eds: S. F. Kistler, P. M. Schweizer), Springer, Dordrecht, The Netherlands **1997**.

[19] J. H. Lee, S. K. Han, J. S. Lee, H. W. Jung, J. C. Hyun, *Korea–Aust. Rheol. J.* **2010**, *22*, 75.

[20] H. Min, M. Kim, S. U. Lee, H. Kim, G. Kim, K. Choi, J. H. Lee, S. Il Seok, *Science* **2019**, *366*, 749.

[21] S. Masi, A. F. Gualdrón-Reyes, I. Mora-Seró, *ACS Energy Lett.* **2020**, *5*, 1974.

[22] M. Kim, G.-H. Kim, T. K. Lee, I. W. Choi, H. W. Choi, Y. Jo, Y. J. Yoon, J. W. Kim, J. Lee, D. Huh, H. Lee, S. K. Kwak, J. Y. Kim, D. S. Kim, *Joule* **2019**, *3*, 2179.

[23] F. Ye, J. Ma, C. Chen, H. Wang, Y. Xu, S. Zhang, T. Wang, C. Tao, G. Fang, *Adv. Mater.* **2020**, *33*, 2007126.

[24] Q. Zhang, G. Ma, K. A. Green, K. Gollinger, J. Moore, T. Demeritte, P. C. Ray, G. A. Hill, X. Gu, S. E. Morgan, M. Feng, S. Banerjee, Q. Dai, *ACS Appl. Energy Mater.* **2022**, *5*, 1487.

[25] K. H. Hendriks, J. J. Van Franeker, B. J. Bruijnaers, J. A. Anta, M. M. Wienk, R. A. J. Janssen, *J. Mater. Chem. A* **2017**, *5*, 2346.

[26] J. W. Lee, Z. Dai, C. Lee, H. M. Lee, T. H. Han, N. De Marco, O. Lin, C. S. Choi, B. Dunn, J. Koh, D. Di Carlo, J. H. Ko, H. D. Maynard, Y. Yang, *J. Am. Chem. Soc.* **2018**, *140*, 6317.

[27] C. Wu, D. Wang, Y. Zhang, F. Gu, G. Liu, N. Zhu, W. Luo, D. Han, X. Guo, B. Qu, S. Wang, Z. Bian, Z. Chen, L. Xiao, *Adv. Funct. Mater.* **2019**, *29*, 1.

[28] E. B. Gutoff, E. D. Cohen, G. I. C. Kheboian, *Coating and Drying Defects*, Wiley-Interscience, New York **1995**.

[29] C. P. Chin, H. S. Wu, S. S. Wang, *Ind. Eng. Chem. Res.* **2010**, *49*, 3802.

[30] M. N. Islam, M. M. Islam, M. N. Yeasmin, *J. Chem. Thermodyn.* **2004**, *36*, 889.

[31] D. Burkitt, R. Swartwout, J. McGettrick, P. Greenwood, D. Beynon, R. Brenes, V. Bulović, T. Watson, *RSC Adv.* **2019**, *9*, 37415.

[32] I. Zizak, *J. Large-Scale Res. Facil. JLSRF* **2016**, *2*, A102.

[33] L. Li, Y. Chen, Z. Liu, Q. Chen, X. Wang, H. Zhou, *Adv. Mater.* **2016**, *28*, 9862.

[34] O. Shargaieva, H. Nässtrom, J. A. Smith, D. Többens, R. Munir, E. Unger, *Mater. Adv.* **2020**, *1*, 3314.

[35] A. Al-Ashouri, A. Magomedov, M. Roß, M. Jošt, M. Talaikis, G. Chistiakova, T. Bertram, J. A. Márquez, E. Köhnen, E. Kasparavičius, S. Levcenco, L. Gil-Escrig, C. J. Hages, R. Schlatmann, B. Rech, T. Malinauskas, T. Unold, C. A. Kaufmann, L. Korte, G. Niaura, V. Getautis, S. Albrecht, *Energy Environ. Sci.* **2019**, *12*, 3356.

[36] A. Czudek, K. Hirselandt, L. Kegelmann, A. Al-Ashouri, M. Jošt, W. Zuo, A. Abate, L. Korte, S. Albrecht, J. Dagar, E. L. Unger, *arXiv preprint arXiv:1906.05028* **2019**.

[37] J. Dagar, K. Hirselandt, A. Merdasa, A. Czudek, R. Munir, F. Zu, N. Koch, T. Dittrich, E. L. Unger, *Sol. RRL* **2019**, *3*, 1900088.

[38] J. Dagar, M. Fenske, A. Al-Ashouri, C. Schultz, B. Li, H. Köbler, R. Munir, G. Parmasivam, J. Li, I. Levine, A. Merdasa, L. Kegelmann, H. Nässtrom, J. A. Marquez, T. Unold, D. M. Többens, R. Schlatmann, B. Stegemann, A. Abate, S. Albrecht, E. Unger, *ACS Appl. Mater. Interfaces* **2021**, *13*, 13022.

[39] A. Al-Ashouri, E. Köhnen, B. Li, A. Magomedov, H. Hempel, P. Caprioglio, J. A. Márquez, A. B. Morales Vilches, E. Kasparavicius, J. A. Smith, N. Phung, D. Menzel, M. Grischek, L. Kegelmann, D. Skroblin, C. Gollwitzer, T. Malinauskas, M. Jošt, G. Matič, B. Rech, R. Schlatmann, M. Topič, L. Korte, A. Abate, B. Stannowski, D. Neher, M. Stolterfoht, T. Unold, V. Getautis, S. Albrecht, *Science* **2020**, *370*, 1300.

[40] H. Köbler, S. Neubert, M. Jankovec, M. Haase, C. Hilbert, M. Topi, B. Rech, A. Abate, *Energy Technol.* **2022**, *10*, 2200234.

[41] D. Liu, Y. Wang, H. Xu, H. Zheng, T. Zhang, P. Zhang, F. Wang, J. Wu, Z. Wang, Z. Chen, S. Li, *Sol. RRL* **2019**, *3*, 1800292.

[42] H. Tsai, R. Asadpour, J. C. Blancon, C. C. Stoumpos, O. Durand, J. W. Strzalka, B. Chen, R. Verduzco, P. M. Ajayan, S. Tretiak, J. Even, M. A. Alam, M. G. Kanatzidis, W. Nie, A. D. Mohite, *Science* **2018**, *360*, 67.

[43] M. V. Khenkin, E. A. Katz, A. Abate, G. Bardizza, J. J. Berry, C. Brabec, F. Brunetti, V. Bulović, Q. Burlingame, A. Di Carlo, R. Cheacharoen, Y. B. Cheng, A. Colsmann, S. Cros, K. Domanski, M. Dusza, C. J. Fell, S. R. Forrest, Y. Galagan, D. Di Girolamo, M. Grätzel, A. Hagfeldt, E. von Hauff, H. Hoppe, J. Kettle, H. Köbler, M. S. Leite, S. (Frank) Liu, Y. L. Loo, J. M. Luther, et al., *Nat. Energy* **2020**, *5*, 35.

[44] E. Unger, G. Paramasivam, A. Abate, *J. Phys.: Energy* **2020**, *2*, 044002.

[45] M. V. Khenkin, K. M. Anoop, I. Visoly-Fisher, S. Kolusheva, Y. Galagan, F. Di Giacomo, O. Vukovic, B. R. Patil, G. Sherafatipour, V. Turkovic, H. G. Rubahn, M. Madsen, A. V. Mazanik, E. A. Katz, *ACS Appl. Energy Mater.* **2018**, *1*, 799.

[46] K. Domanski, E. A. Alharbi, A. Hagfeldt, M. Grätzel, W. Tress, *Nat. Energy* **2018**, *3*, 61.

[47] M. Du, S. Zhao, L. Duan, Y. Cao, H. Wang, Y. Sun, L. Wang, X. Zhu, J. Feng, L. Liu, X. Jiang, Q. Dong, Y. Shi, K. Wang, S. F. Liu, *Joule* **2022**, *6*, 1931.

[48] M. Fenske, C. Schultz, J. Dagar, F. U. Kosasih, A. Zeiser, C. Junghans, A. Bartelt, C. Ducati, R. Schlatmann, E. Unger, B. Stegemann, *Energy Technol.* **2021**, *9*, 2000969.

[49] C. Schultz, M. Fenske, J. Dagar, A. Zeiser, A. Bartelt, R. Schlatmann, E. Unger, B. Stegemann, *Sol. Energy* **2020**, *198*, 410.

[50] J. Hidalgo, C. A. R. Perini, A. F. Castro-Mendez, D. Jones, H. Köbler, B. Lai, R. Li, S. Sun, A. Abate, J. P. Correa-Baena, *ACS Energy Lett.* **2020**, *5*, 3526.

[51] A. D. Edelstein, M. A. Tsuchida, N. Amodaj, H. Pinkard, R. D. Vale, N. Stuurman, *J Biol Methods* **2014**, *1*, e10.

[52] P. Würfel, W. Ruppel, *J. Lumin.* **1981**, *24–25*, 925.

[53] T. Kirchartz, J. A. Márquez, M. Stolterfoht, T. Unold, *Adv. Energy Mater.* **2020**, *1904134*, 1904134.

[54] D. M. Többens, S. Zander, *J. Large-Scale Res. Facil. JLSRF* **2016**, *2*, 1.